Journal of Glaciology



Article

Cite this article: Kerr T, Purdie H, Bealing P, Schumacher B, Katurji M, Datta R, Zawar-Reza P (2025) Crevasse effects on glacier surface temperature from thermal imagery. *Journal of Glaciology* **71**, e51, 1–12. https://doi.org/10.1017/jog.2025.7

Received: 18 July 2024
Revised: 15 January 2025
Accepted: 16 January 2025

Keywords:
Crevasse; snow surface temperature; thermal imagery

Corresponding author: Heather Purdie;
Email: heather.purdie@canterbury.ac.nz

© The Author(s), 2025. Published by Cambridge University Press on behalf of International Glaciological Society. This is an Open Access article, distributed under the terms of the Creative Commons Attribution licence (http://creativecommons.org/licenses/by/4.0), which permits unrestricted re-use, distribution and reproduction, provided the original article is properly cited.

Crevasse effects on glacier surface temperature from thermal imagery

Tim Kerr[1,2], Heather Purdie[1], Paul Bealing[1], Benjamin Schumacher[3], Marwan Katurji[1], Rajasweta Datta[4] and Peyman Zawar-Reza[1]

[1]School of Earth and Environment, University of Canterbury, Christchurch, New Zealand; [2]Rainfall.NZ, Christchurch, New Zealand; [3]Earth Observation Data Centre for Water Resources Monitoring GmbH, Vienna, Austria and [4]World Resources Institute, India, New Delhi, India

Abstract

Thermal imagery was collected for 26 hours over a crevassed region within the accumulation zone of the Haupapa/Tasman Glacier, New Zealand. During the night, the imaged snow surfaces associated with crevasses cooled slower than non-crevassed surfaces resulting in temperature differences of several degrees. Night surface temperature varied across the non-crevassed areas to a smaller degree, primarily in relation to slope. The surface temperature difference between crevassed and non-crevassed surfaces is primarily attributed to the reduced sky-view of crevasses so that a large proportion of longwave radiation is not emitted away from the glacier but is received by opposing crevasse walls. Possible additional causes are that crevasses trap warm air which enables greater sensible heat transfer, crevasses have greater conduction of heat from isothermal glacier ice as a result of limited insulating snow, and crevasse walls have greater amounts of liquid water which delays the onset of surface freezing.

1. Introduction

Measurements on the Haupapa/Tasman Glacier (hereafter Tasman Glacier), New Zealand, show that air within crevasses can sometimes be warmer than the out-of-crevasse air over the glacier, particularly with respect to wide crevasses oriented favourably for shortwave radiation receipt or for crevasses running parallel to windflow (Purdie and others, 2022). However, other published in situ crevasse temperature measurements (summarised in Table 1) have described the air temperature as being both cooler and warmer than the out-of-crevasse air (Cook, 1956; Meier and others, 1957; Harrison and others, 1998; Bhardwaj and others, 2016). For example, Cook (1956) found that for an enclosed crevasse on the western margin of the Greenland ice sheet (~ 78°N) in summer, the daytime temperature of air inside the crevasse at 6 m depth was generally 4°C cooler than the air temperature out-of-crevasse, with little variation over time. In contrast, in another Greenland crevasse (76°N), which was open to the atmosphere, the air temperature inside the crevasse was found to be warmer than the air temperature overlying the glacier surface (Meier and others, 1957; Pings, 1961). In addition, air temperatures inside crevasses were often 2°C warmer than the adjacent crevasse walls, creating a positive energy flux towards the glacier ice (Pings, 1963). Harrison and others (1998) also found that crevasses impacted glacier ice temperature, but in their case, it was a cooling rather than a warming effect. They measured summer air temperature inside four crevasses associated with Ice Stream B in Antarctica (83°S), finding that air inside the crevasse was considerably colder (by up to 25°C) than air overlying the glacier surface. More recently, Bhardwaj and others (2016) found that for the Shaune Garang Glacier of India (31°N), the in situ air temperature measured at 10 m depth within a crevasse was ~ 5°C cooler than the air temperature outside of the crevasse.

As an alternative to in situ measurements, thermal infrared imagery provides another method to characterise crevasse temperature fields (Kinar and Pomeroy, 2015). From a radiative perspective, snow surfaces are characterised by high emissivity (0.98–0.99) and low thermal conductivity (Oke, 1987; Kinar and Pomeroy, 2015). Combined, these characteristics mean that snow emits almost all of the thermal radiation it absorbs making it an ideal medium for infrared temperature measurement. It is important to remember that thermal infrared temperature is only a measure of the very top (1 mm) of the snow surface (Dozier and Warren, 1982; Kraaijenbrink and others, 2018), rather than air temperature immediately above the snow surface, or the internal temperature of the snow (Kinar and Pomeroy, 2015). Nonetheless, these surface temperature measurements can help understand glacier energy processes, including those associated with crevasses. Unfortunately, as with air temperatures, published thermal infrared

measurements are not in agreement about the temperature differential between crevasse and out-of-crevasse temperatures.

Thermal infrared measurements of crevasses (summarised in Table 1) can be ground-based (e.g. Aubry-Wake and others, 2015), aerial (e.g. Rinker, 1975; Rossini and others, 2023), or from satellites (e.g. Bhardwaj and others, 2016). Ground-based thermal infrared imaging of crevasses by Aubry-Wake and others (2015) on the Cuchillacocha Glacier in Peru (9°S) found that crevassed areas were on average 1.2°C warmer than surrounding glacier surfaces, which they attributed to increased absorption of shortwave radiation as described by Pfeffer and Bretherton (1987). Aerial sensors were used on the Greenland ice sheet (76°S) during the early afternoon in March (winter) of 1962 to identify crevasses covered over by snow, which displayed temperatures 24°C warmer than the surrounding −35°C surfaces. They attributed this to the convection and conduction of relatively warm air from inside the crevasse up through the snow bridges (Rinker, 1975). In contrast, Rossini and others (2023) found that when using infrared cameras on aerial platforms on the Zebrú Glacier in Italy (46.5°N) daytime thermal signatures of crevasses in the ablation area were relatively indistinguishable from surrounding clean ice when compared to the high thermal contrast of debris-covered ice. The use of satellite observations specifically for crevasse detection by temperature was carried out by Bhardwaj and others (2016) on the Shaune Garang Glacier in India (31°N). Crevasses were able to be detected using their manually confirmed cooler temperatures with respect to the other glacier surfaces, thereby enabling crevasse mapping.

Observations using thermal infrared imagery need to be assessed with care to ensure that temperature field variations include consideration of camera calibration, lens effects, sensor drift and radiative characteristics of the atmosphere, for example, water vapour (Meier and others, 2011; Kraaijenbrink and others, 2018; Pestana and others, 2019; Arioli and others, 2024). One approach to minimise these issues is to consider measurements from a relative perspective, assuming that the majority of issues affect all image pixels equally and that inter-pixel variation is temporally stable and relatively small. This approach has been used by Christen and others (2012); whereby each pixel's temperature in each image is subtracted from the image's average temperature. Through this differencing, any image-wide sensor drift or calibration effects are removed. The cost of this approach is that absolute temperatures are not obtained, so insights associated with specific temperature thresholds of interest (e.g. 0°C) are lost. A complicating factor with highly oblique imagery particularly over complex terrain is that individual image pixel's fields of view and surface angle can vary considerably across an image and impact camera-received energy. In particular, emissivity variations associated with viewing angles can result in temperature errors of up to 3°C (Dozier and Warren, 1982), although this effect was found to be less significant for viewing angles less than 50° (Litwa, 2010) and is surface dependent (Hori and others, 2006). In mountainous terrain, large variability in snow surface temperature is created by topographic effects on incident radiation, specifically slope angle, aspect and shading (Arnold and others, 2006; Robledano and others, 2022). These effects need to be considered and quantified to ensure that the primary cause of temperature variation is correctly attributed, even if relative (e.g. Kraaijenbrink and others, 2018) rather than absolute (e.g. Arioli and others, 2024) temperatures are being considered.

Glacier melt modelling often exploits the fact that the temperature of melting snow or ice surfaces is 0°C (Hock, 2005). Indeed, this very characteristic of a melting snow surface has been previously used to bias correct thermal infrared imagery (Pestana and others, 2019). However, such an assumption can be problematic where snow surfaces cool to sub-zero temperatures overnight (Bilish and others, 2018). Targeted field studies utilising thermal infrared imagery are well suited to improving the understanding of the spatial and temporal variability of surface temperatures on glaciers (Aubry-Wake and others, 2015), particularly in accumulation areas, which can exhibit considerable diurnal temperature fluctuations. During winter months, crevasses in glacier accumulation areas become filled or covered with snow creating a homogeneous snow surface, but as melting resumes, crevasses are re-exposed at the glacier surface. As the climate continues to warm and alpine snowpacks thin (Hock and others, 2019), the duration of time that crevasses remain 'open' and exposed at the glacier surface is increasing (Purdie and Kerr, 2018), meaning that their influence on glacier surface energy balance is also increasing (Purdie and others, 2022).

Modelling the crevasse impacts on glacier energy receipt provides some insights into relative crevasse temperatures. Pfeffer and Bretherton (1987) found 'V' shaped crevasses could absorb more direct shortwave radiation energy through their opening than an equivalent-sized flat surface as a result of repeat reflections within the crevasses. Further, the crevasse orientation has an impact as discerned from the modelling efforts of Cathles and others (2011), whereby east-west-oriented 'V' crevasses had enhanced melt modelling with respect to north-south crevasses, particularly in lower latitudes. Cathles and others (2011) also highlighted the importance of crevasse depth, with deeper crevasses absorbing more energy than shallow crevasses.

Previous studies of the effect of crevasses on temperature (reviewed in Colgan and others, 2016) have highlighted the ambiguity created by crevassed terrain for melt modelling, with observations showing that they may be warmer or cooler than the surrounding snow surfaces (Table 1). To improve understanding and generalisation of these findings, additional observations of crevasse temperatures are required together with links to physical characteristics and processes.

This contribution explores how crevassed topography influences surface temperature in a glacier accumulation area at high spatial and temporal resolution. Specifically, we utilise ground-based thermal infrared imagery to characterise the relative temperature differences between crevassed and non-crevassed surfaces, focusing on short-term temporal variability. Observed variations in surface characteristics as well as the spatial and temporal variations in temperature are used to assist in establishing process-orientated explanations for the observed crevasse temperatures.

While the primary research objective of this field experiment was to determine the influence of crevasses on surface temperature, the timing of our field campaign in 2020 coincided with notable discolouration of the snow surface. The source of this discolouration was Australian dust, which had been transported across the Tasman Sea under favourable meteorological conditions (Winton and others, 2024). It is well recognised that deposition of light-absorbing impurities reduces snow and ice albedo, which enhances shortwave radiation absorption, and in turn, exacerbates surface melting (e.g. Oerlemans and others, 2009; Di Mauro and others, 2015). Due to its differing emissivity, dust is distinguishable from snow in the thermal infrared wavelengths (Bowen and Vincent, 2021). Therefore, we took this opportunity to also explore any variability in snow surface temperature associated with the dusty

https://doi.org/10.1017/jog.2025.7 Published online by Cambridge University Press

Table 1. Crevasse temperature observations from previous studies

Variable	Crevasse condition	Description	Location	Latitude	Citation
Air T.	Warmer	Crevasse air warmer than out-of-crevasse air.	Tasman Glacier, New Zealand	43°S	Purdie and others (2022)
Air T.	Cooler	Enclosed crevasse air cooler than out-of-crevasse air.	Greenland ice sheet	~78°N	Cook (1956)
Air T.	Warmer	Crevasse air warmer than adjacent glacier ice.	Blue Ice Valley, Greenland	76°N	Meier and others (1957); Pings (1961, 1963)
Air T.	Cooler	Summer crevasse air 25°C cooler than out-of-crevasse air.	Ice Stream B, Antarctica	83°S	Harrison and others (1998)
Air T.	Cooler	Crevasse air ~5°C cooler than out-of-crevasse air.	Shaune Garang Glacier, India	31°N	Bhardwaj and others (2016)
Infrared	Warmer	Crevasse walls 1.2°C warmer than non-crevassed surfaces.	Cuchillacocha Glacier, Peru	9°S	Aubry-Wake and others (2015)
Infrared	Warmer	Covered over crevasse lids 24°C warmer than non-crevassed surfaces.	Greenland ice sheet	76°N	Rinker (1975)
Infrared	No difference	Crevassed areas relatively indistinguishable from non-crevassed areas.	Zebrú Glacier, Italy	46.5°N	Rossini and others (2023)
Infrared	Cooler	Crevassed areas cooler than non-crevassed areas.	Shaune Garang Glacier, India	31°N	Bhardwaj and others (2016)

snow surfaces captured by our ground-based thermal infrared imagery.

2. Study site

Tasman Glacier (Fig. 1) is the largest glacier in New Zealand containing ~1/3 of the country's ice volume (Chinn, 2001). This work continues a long history of Tasman Glacier glaciological investigations (e.g. Lendenfeld, 1884; Cotton, 1941; Skinner, 1964; Kirkbride, 1995; Purdie and Fitzharris, 1999; Röhl, 2008; Purdie and others, 2011, 2018). The accumulation area of the Tasman Glacier receives ~4 m w.e. of snow every year (Purdie and others, 2011), from 6 m w.e. of precipitation (Kerr and others, 2011) and ~1.1 m w.e. of melt (Purdie and others, 2018). Precipitation can fall at any time of year, primarily as snow, but also as rain. Snow accumulation occurs from April to November and ablation dominates from November to March (Purdie and others, 2018). Crevasses occur across much of the glacier surface. In the lower ablation area, which is heavily debris-covered, crevasses are predominately found near margins and shear zones and remain snow-free most of the year (Fig. 1b). Above this region, the glacier transitions to clean ice, with the many crevasses found near the debris-transition as the glacier spreads to fill the valley. Crevasses in the upper ablation area are relatively shallow (~5 m) and usually become snow-filled in the winter months (i.e. July–September). The long-term equilibrium line is located at ~1790 m a.s.l. (Lorrey and others, 2022). The accumulation area is heavily crevassed (Fig. 1c). Crevasses in this region generally exceed 20 m depth (Purdie and others, 2022) and are snow-filled/covered from late July to early December. Depending on the seasonal weather patterns, crevasses in the accumulation area are usually well-exposed at the surface by January.

The total accumulation area of Tasman Glacier covers 16 km^2 (excluding tributaries joining the glacier below the equilibrium line), but this investigation focused on the broad (1 km) and relatively flat ($< 20°$) eastern portion of the accumulation area (Fig. 1b and c). In this location, the glacier surface is ~2300 m a.s.l., with the immediately surrounding ridges and peaks ranging from 2400 to 2800 m a.s.l. Discolouration of the snow surface by dust in the accumulation area was widespread though not complete (Fig. 1c). Due to the broad nature of the site, topographic shading was not of concern in the area of interest (Fig. 1c).

3. Data and methods

Thermal images were collected over 26 hours in late summer from 19:00 (local time) on the 24th February 2020 until 21:00 on the 25th February using an Optris PI450 single-band thermal infrared camera (Table 2; Optris, 2020) mounted on a rocky ridge overlooking a crevasse field in the upper region of the Tasman Glacier (Figs. 1 and 2). The camera had an internal reference shutter (flat field correction) that covered the sensor at regular intervals for continual camera calibration adjustment. The camera body was thermally regulated to be within a temperature range of 15–25°C , though the system itself could operate from −20 to 40°C . The system used up to 70 W, supplied by a lead-gel 24 V battery kept charged by a methanol fuel cell. The full system encompassing the camera, enclosure, mounting tripod, battery and fuel cell weighed ~20 kg. The camera was sited so that its field of view minimised topographic complexities, focusing on a portion of the glacier's accumulation area that was relatively flat ($< 20°$) and away from peaks and rock buttresses (Fig. 2). The images were collected at 20 Hz and averaged to 10 minutes in post-processing to align with the data from two automatic weather stations. Three aluminium plates (0.5 m x 0.5 m), intended as control points for the thermal imagery, were placed within the crevasse field and oriented towards the camera.

A photogrammetric survey of the study site was carried out with a DJI Phantom 4 RTK remotely piloted aerial system that has an integrated camera and GNSS. Camera positions were corrected in real-time using a DJI D-RTK2 base station to have relative accuracy of 4 cm in the vertical and 6 cm in the horizontal (Table 2). The survey was flown at 120 m above ground level, with front and side photo overlap of 75 % resulting in a pixel resolution of 3.3 cm. Agisoft Metashape software (version 1.6.5) was used to align all photos to generate an orthoimage (3.3 cm $pixel^{-1}$) and a digital elevation model (DEM, 13 cm $pixel^{-1}$). Both the orthoimage and DEM were projected to NZ Transverse Mercator (EPSG:2193) with heights above the WGS84 ellipsoid (Fig. 1c).

The thermal images were orthorectified using the *cam_gen* and *mapproject* commands from the Ames Stereo Pipeline software (Beyer and others, 2018), following Arioli and others (2024). The orthorectification process used the DEM to triangulate the thermal image pixels to geographic space. The process also used control points with known locations in both the DEM and the thermal

https://doi.org/10.1017/jog.2025.7 Published online by Cambridge University Press

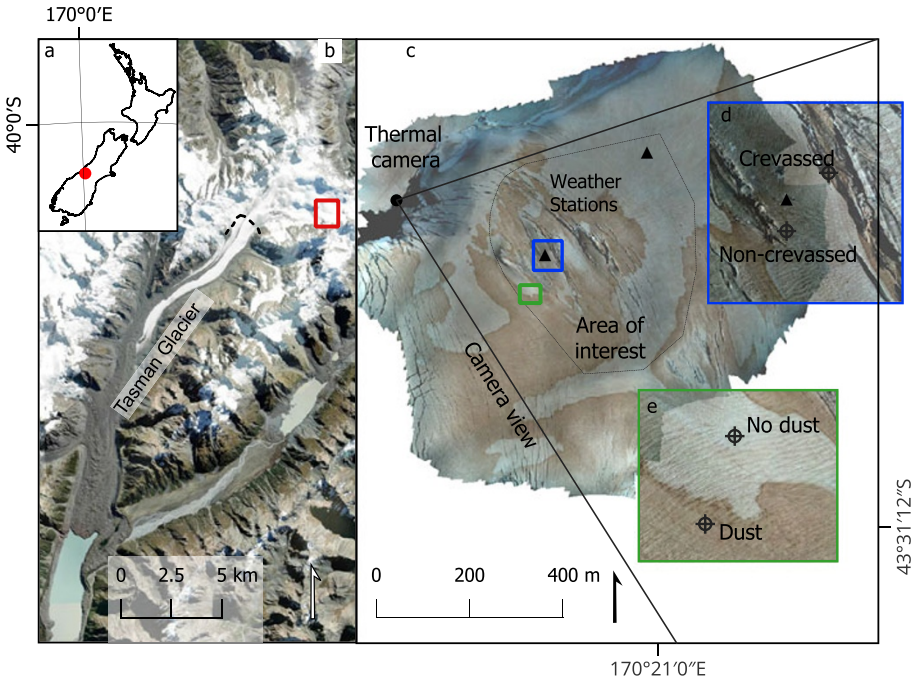


Figure 1. (a) Location of Tasman Glacier in the South Island of New Zealand, (b) location of the study area (red box) with respect to the Tasman Glacier, and equilibrium line (black dashed line) indicating the separation between the glacier's accumulation and ablation areas, (c) orthoimage of camera view area showing locations of the thermal camera (dot), two weather stations (triangles), the primary area of interest (dotted line), the area of the crevasse/non-crevassed thermal image sample sites (blue box) and the area of the dust/no dust thermal image sample sites (green box), (d) detail of crevasse/non-crevassed thermal image sample sites and (e) detail of dust/no dust thermal image sample sites.

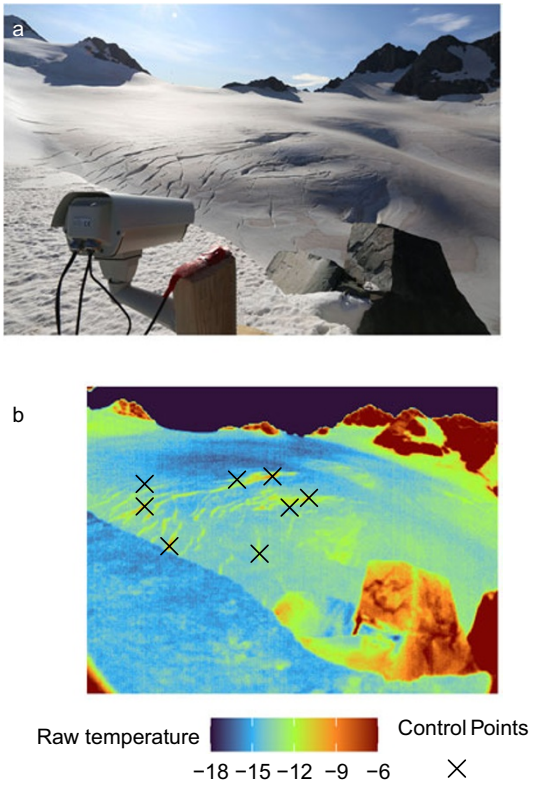


Figure 2. (a) View from the camera location at 08:00 and (b) example thermal image (as uncorrected temperatures) from 03:00 with crevasses seen as relatively warm areas, locations (X) used for control points in orthorectification.

camera images. Control points were taken from features seen in both the thermal imagery and the aerial orthoimage. A total of eight well-distributed control points were used (two surveyed reflectors and six crevasses, Fig. 2b). One of the three aluminium reflector plates, intended as thermal image control points, was found to be too far from the thermal camera (and consequently too small), to be unambiguously identified in the thermal imagery. The location uncertainty of the crevasse-control points was estimated as $\pm$ 2 pixels on the thermal imagery and $\pm$ 2 m on the aerial orthoimage. The resolution of the orthorectified thermal images was set to 2 m, representative of the field of view of a single thermal camera image pixel near the edge of the area of interest. Bicubic interpolation was used to convert from the thermal camera's projected resolution (variable across the field of view) to the 2 m orthorectified resolution. Finally, the orthorectified thermal images were clipped to the area of interest and masked to the thermal camera's viewshed. A comparison of the orthorectified thermal images with the aerial orthoimage indicated that the orthorectification had a horizontal spatial error of $\pm$ 5 m. Other errors associated with lens distortion and sensor array variations were not accounted for or assessed, though the image analysis was restricted to the central part of the thermal camera view where some of these effects are minimised.

Two weather stations were installed. One within the crevasse field, and the other on a smooth snow surface (Fig. 1c). Each weather station measured outgoing and incoming longwave radiation, temperature, humidity, wind speed and shortwave radiation (Purdie and others, 2022, Table 1, p. 414). The outgoing longwave radiation measurements were converted to surface temperature using Stefan–Boltzmann's law and a snow emissivity of 0.99. The longwave sensors have a temperature sensitivity of $< 5\%$ (over a temperature range from −15 to 45°C) and a field of view of 150° (Apogee, 2020), which, from their position mounted 1.4 m above the surface, would have included the aluminium legs of the mounting tripods. Correction of the errors associated with the longwave sensor's view field and temperature sensitivity was not applied, except that the temperature series derived from the longwave sensor's observations was lowered by 4°C so that the maximum was 0°C to match the melting snow surface observed during the day of operation following the approach of Pestana and others (2019).

A temperature time series was extracted from the orthorectified thermal imagery for a non-crevassed flat surface adjacent to

https://doi.org/10.1017/jog.2025.7 Published online by Cambridge University Press

Table 2. Equipment specifications

Description	Make	Model	Attribute	Specifications
Infrared camera	Optris	Pi450	Accuracy	2°C
			Wavelength range	7.5–14 μm
			Frequency range	21–37 THz
			Temperature sensitivity	$\pm$0.05 %/°C
			Precision	40 mK
			Field of view	80° x 54°
			Image resolution	382 x 288 pixel
			Pixel size at 550 m	2 x 1.8 m
Longwave sensor	Apogee	SN-500	Accuracy	$\pm 5\%$
			Temperature sensitivity	$< 5\%$ from −15 to 45°C
			Field of view	150°
Remotely piloted aerial system	DJI	Phantom 4 RTK		
Visible aerial camera	DJI	Phantom 4 RTK	Image resolution	3 cm
Aerial GNSS	DJI	Phantom 4 RTK	Relative accuracy	4 cm vertical, 6 cm horizontal
GNSS Base Station	DJI	D-TK2		

the lower weather station (Fig. 1d). This temperature series was compared to that derived from the outgoing longwave sensor's observations, and the difference time series was used to correct pixel temperatures in the orthorectified thermal image series. This temperature correction did not affect the within-image temperature variation which was the primary interest for the purposes of assessing the impact of crevasses.

To analyse the magnitude and timing of any surface temperature differences between a crevassed and non-crevassed glacier surface, a representative crevasse wall temperature was selected from the corrected imagery and compared to the corrected surface temperature of a non-crevassed area (Fig. 1d). This initial 'point' comparison (3 x 3 pixel sample) was followed by an assessment of the full area of interest, requiring an areal classification into crevasses and non-crevasses. This was achieved by classifying the visible 3 cm orthoimage using a threshold of 80 (of 255) on each of the red, green and blue colour bands. This high-resolution classification was resampled to 2 m to match the resolution of the orthorectified thermal images. A 2 m pixel was classified as a crevasse if more than 50 % of the contributing 3 cm pixels were classified as crevasses. A 2 m pixel was classified as non-crevassed, if it was at least 3 m from a crevassed pixel. This ensured that the non-crevassed areas were well clear of any crevasses. To enable comparison to the orthorectified thermal images, the crevasse/non-crevassed classifications were masked to the area of interest (Fig. 1c) and to the camera viewshed. In addition to contrasting crevassed and non-crevassed pixels, dust and no dust thermal imagery temperatures were compared based on 3 x 3 pixel samples of representative locations (Fig. 1e).

In order to have confidence in the attribution of any detected differences in surface temperature between crevassed and non-crevassed terrain, it was important to assess the impact of potential topographic-induced variability (e.g. Arnold and others, 2006; Olson and others, 2019). Therefore, the DEM was further processed using the R software language (R Core Team, 2021) and the Terra package in particular (Hijmans, 2024) to determine slope, aspect, distance to camera, horizontal angle to camera, vertical angle to camera and camera viewshed. The camera viewshed excluded those parts of the crevasses that cannot be seen from the camera. Finally, each of these derived surface characteristics was binned into 20 equal parts and the mean temperature of the non-crevassed areas was determined for each bin and each 10-minute thermal image.

4. Results

The weather during the measurement period was generally calm and clear with air temperatures above 0°C . The air temperature, shortwave radiation, longwave radiation and wind speed, as measured at the lower (southern) weather station, sited among some crevasses, are shown in Fig. 3. The break in the shortwave radiation mid-afternoon of the 25th is from temporary cloud shadow.

The infrared images captured through the night clearly show crevassed regions warmer than the surrounding glacier surface with $>$ 4°C contrast (Fig. 2b). However, the daytime images showed very little contrast ($<$ 2°C). Therefore, when reporting the results of the spatial analysis below, comparisons are often made between images recorded at 03:00 (strong contrast) and images recorded at 15:00, when there was little contrast. Raw image temperatures were ∼5°C colder than 0°C for the glacier surface during the day when surface melting was observed.

A comparison between the thermal image raw temperature and the lower weather station surface temperature (based on the longwave sensor measurements) is depicted in Fig. 4a. A strong linear relationship is shown, confirming that the thermal images provide a valid index of temperature. The relationship has about $\pm$1°C of uncertainty. Not shown is the regular saw-tooth variability of the raw thermal imagery temperatures attributed to the thermal camera's repeating auto-calibration. These calibration step changes vary in magnitude depending on the rate of change of the ambient temperature but have a mean amplitude of 0.5°C, which indicates they are a large component of the uncertainty in the relationship between the surface temperatures obtained from the raw thermal images and the weather station.

Overnight, the sample of pixels associated with a crevassed area were found to cool more slowly than the non-crevassed sample pixels (Fig. 4b). Temperatures at both locations stabilised at approximately 03:00, but with a temperature difference of 2.5°C . Shortly before 09:00, both sample locations warmed rapidly. After this, both locations had similar temperatures for the remainder of the observation period. The dust and no dust sample pixels showed similar temperatures for most of the measurement period (Fig. 4c). The temperature difference between the dust and no dust sample pixels was small, and within the 0.5°C assumed for intra-image pixel temperature uncertainty, indicating any impact of the dust on surface temperature under the conditions experienced is at the limits of detection of the thermal camera.

The results of our image classification identified 161 pixels as crevassed (Fig. 5c), while 31503 pixels were considered to be largely

https://doi.org/10.1017/jog.2025.7 Published online by Cambridge University Press

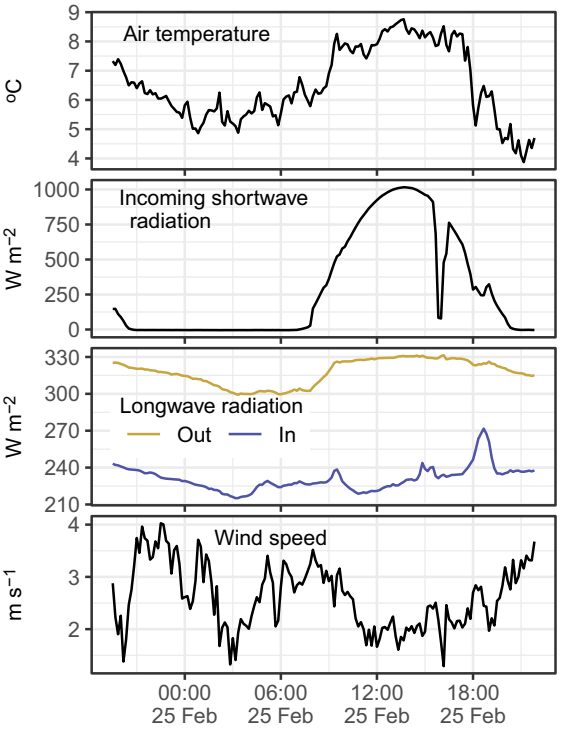


Figure 3. Measurements from the lower (southern) weather station sited among crevasses. Refer to Fig. 1c for location of the weather station.

crevasse free. Most of the crevasses were approximately perpendicular to the camera's forward-pointing direction, so the camera's view of the crevasses was generally only the top part of the far crevasse wall. After orthorectification, these near-vertical surfaces are relatively small compared to horizontal surfaces but still influence the pixel value. The camera viewshed shown in orange in Fig. 5c explicitly omitted the parts of the crevasses that cannot be seen from the camera.

After temperature correction, the 03:00 thermal image (Fig. 5a) had a minimum temperature of −9°C on a smooth snow surface, north-east of the crevasses, while the maximum temperature (−2°C) was associated with the crevasses.

Extending our point analysis to the full area of interest, we again found that the 03:00 temperature distribution of the crevasse class was warmer compared to the non-crevassed class, with a mean temperature difference of 1.4°C (Fig. 6). At 03:00, the median temperature of the crevasse class was warmer than the upper quartile of the non-crevassed class. Both a two-sided t-test ($t = 13.5$, $p < 0.001$) and a non-parametric Mann-Whitney U-test ($W = 4\ 096\ 372$, $p < 0.001$) further indicate that the surface temperature of the two classes were statistically distinct. At 15:00, the distribution of the temperatures of the crevassed and non-crevassed pixels was similar, with a difference of the means of the sample sets of only 0.06°C .

The surface characteristics created from the DEM for the area of interest are shown in Fig. 7. Crevasses are most easily distinguished from the slope and aspect characteristics where they show in high contrast to the relatively horizontal non-crevassed surfaces (Fig. 7b and c). Only the widest crevasses can be determined from the elevation and vertical-angle-to-camera characteristics (Fig. 7a and e). No indication of crevasses can be discerned from the horizontal-angle-to-camera or distance-to-camera characteristics (Fig. 7d and f).

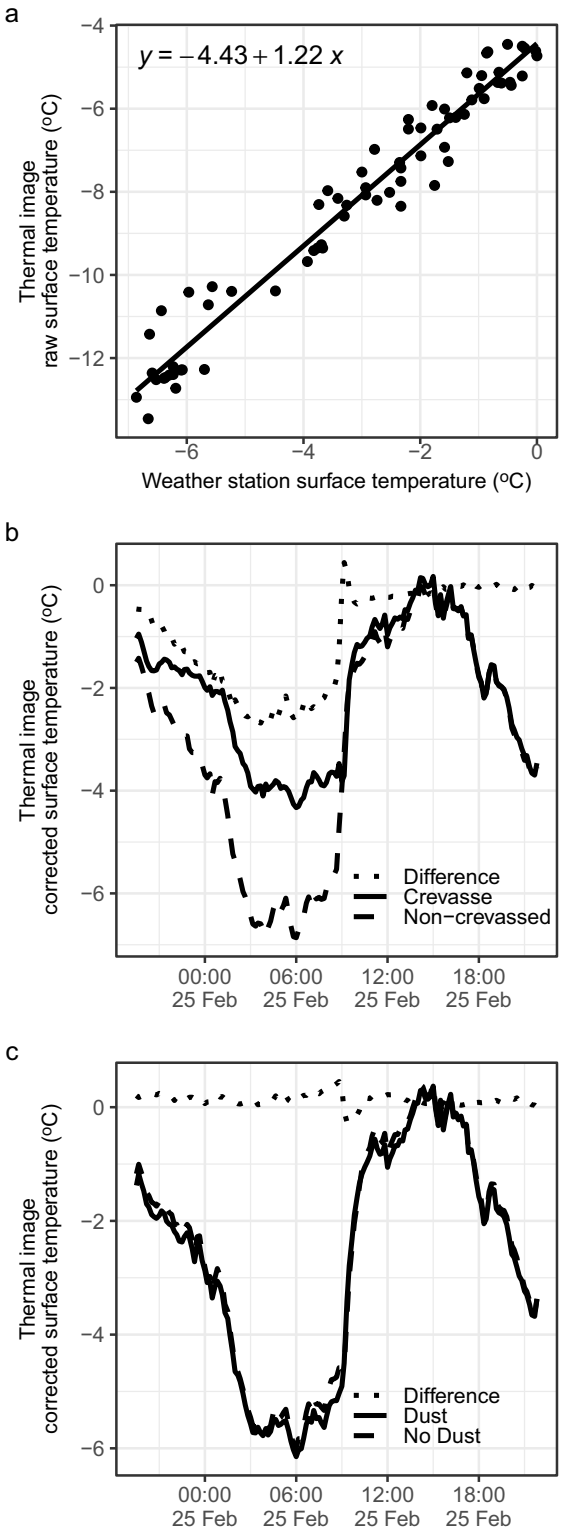


Figure 4. (a) Thermal image raw temperature at the non-crevassed pixel sample site (Fig. 1d) compared to surface temperature derived from the lower weather station's longwave measurements, (b) time series of corrected surface temperature for the crevasse and non-crevassed pixel sample sites (Fig. 1d), with their difference, and (c) time series of corrected surface temperatures for the dust and no dust pixel sample sites (Fig. 1e), with their difference (no dust minus dust).

Figure 8 shows how surface temperature over non-crevassed areas varied with each surface characteristic. For all the surface characteristics, there was very little variation during the daytime.

https://doi.org/10.1017/jog.2025.7 Published online by Cambridge University Press

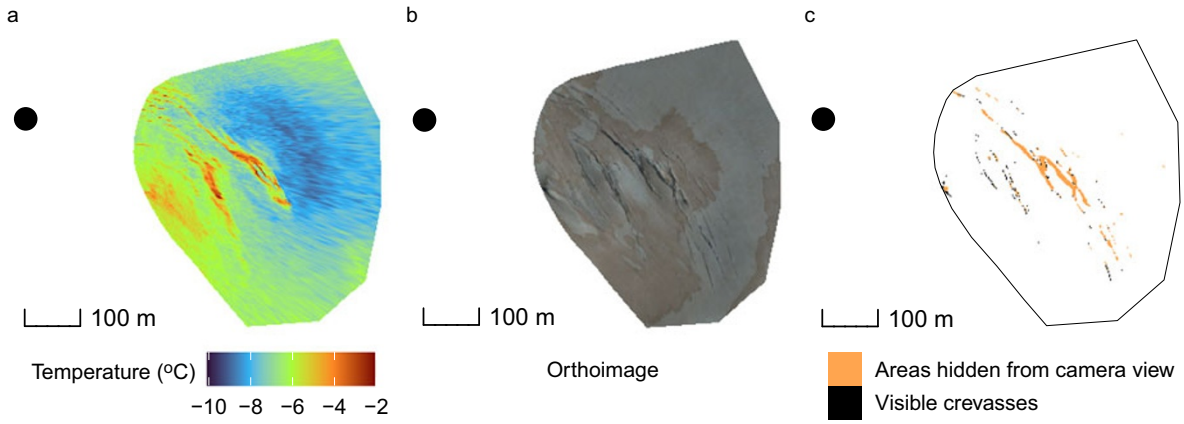


Figure 5. (a) Orthorectified thermal image from 03:00 local time of the crevassed area of interest, with corrected temperatures, (b) the RGB orthoimage for the same area and (c) pixels classified as crevasses within view of the camera (black) and areas hidden from the camera view because they are shaded by a crevasse wall (orange). The black circle represents the location of the camera.

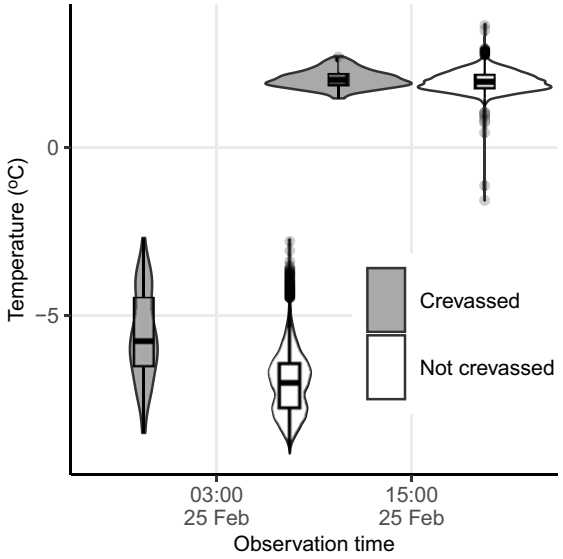


Figure 6. Surface temperature distributions for crevassed and not crevassed pixels at 03:00 and 15:00 on 25 February. The violins are scaled so that they have equal areas.

At night, higher elevations and lower sloped surfaces were cooler (Fig. 8a and b). Aspects facing away from the camera (i.e. from 60 to 180°) were warmer during the night than aspects facing the camera (Fig. 8c). Surfaces due east of the camera (i.e. 90°) were warmer during the night (Fig. 8d). Lastly areas with shallower vertical angle from the camera, and further away, were cooler during the night (Fig. 8e and f)

5. Discussion

Previous work demonstrated that for the Tasman Glacier, air temperatures inside crevasses were frequently positive (Purdie and others, 2022). Given that the temperate ice is at its melting point, that finding indicated that crevasses will at times be loci of mass loss, which usually goes unaccounted for. This work built on those initial findings by using ground-based oblique thermal imagery to assess snow surface temperature variability associated with crevasses at a broader spatial scale. Our results are in agreement with that initial study, finding a statistically significant difference between the snow surface temperature of crevassed and non-crevassed locations, with the crevassed locations at times being on average 1.4°C warmer (Fig. 6). Opportunistic comparison of the effect of dust on surface thermal image temperatures was not able to robustly distinguish it from dust-free surfaces, despite its clear effect on surface colour. Care was required in the interpretation of the use of thermal infrared observations to map snow and ice temperature in complex terrain, reflective of previous similar undertakings (e.g. Aubry-Wake and others, 2015; Kraaijenbrink and others, 2018; Pestana and others, 2019; Arioli and others, 2024).

The analyses presented assumed that the within-image relative temperature differences provided by the infrared camera were reasonable, even if the absolute temperatures were not. Indeed, during the day, the raw infrared camera temperatures were ∼−6°C for flat melting snow surfaces that would have been 0°C . This magnitude of error is more than would be expected from calibration and atmospheric effects alone. Similar offsets have been reported for infrared camera use in glacier environments by Aubry-Wake and others (2015) which in their case was attributed to unusual atmospheric conditions not present on the Tasman Glacier. A possible cause of the offset was the low ambient temperature of the camera enclosure's view window, which impacts that Arioli and others (2024) assessed could lead to the magnitude of error observed. In addition, the camera uses a single emissivity value for its internal conversion of received energy to temperature. An emissivity setting that was on average 0.05 too high would lead to a 3°C low bias in temperature, so a high-biased emissivity setting may explain a component of the offset. The use of the weather station's outgoing longwave radiation measurements to bias correct the infrared camera was foiled by the wide field of view of the instrument, and the limitations of its mounting on the weather station. Ideally, these issues would have been resolved, but the nature of the fieldwork setting was not conducive to repeated measurement campaigns to resolve these issues after they were identified during post-processing.

Consideration of relative within-scene temperatures rather than absolute temperatures assumes that the errors are largely consistent for the entire view. While this assumption is not perfectly true, Arioli and others (2024) found for the similar Optrix Pi640 thermal camera that most pixels of a single image of a black body were within 0.5°C of each other and that the difference between

https://doi.org/10.1017/jog.2025.7 Published online by Cambridge University Press

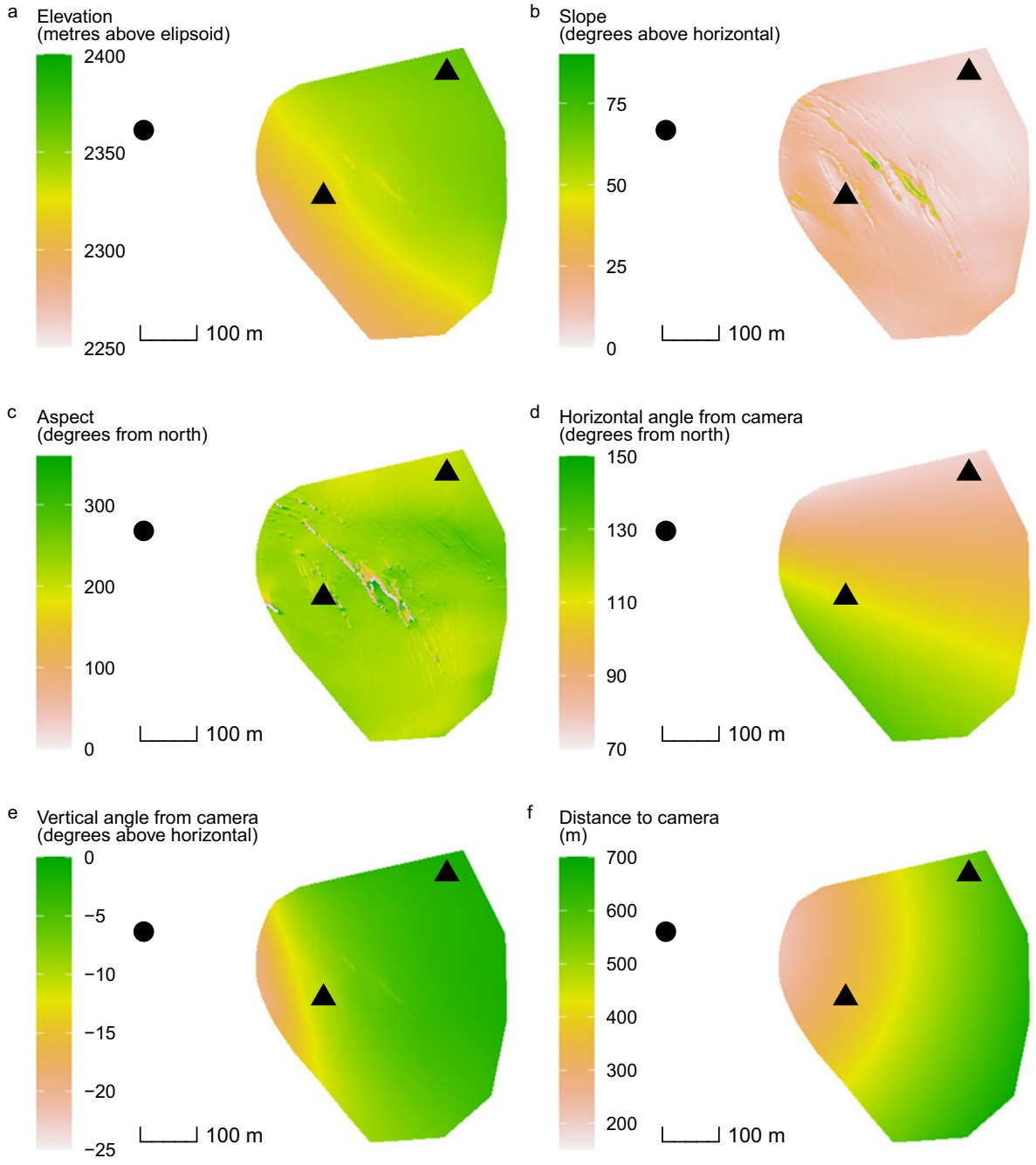


Figure 7. Surface characteristics of the crevassed area of interest. (a) elevation, (b) slope, (c) aspect, (d) horizontal angle from camera, (e) vertical angle from camera and (f) distance to camera. The black circle gives the relative location of the camera. The black triangles are where the weather stations were located.

pixel response within an image was stable over time. With this in mind, temperature variations across an image much larger than 0.5°C have been attributed to real temperature variations at the observed surfaces and not artefacts of camera limitations. Indeed, unlike Arioli and others (2024), no attempt at correction of image distortion, sensor temperature sensitivity, faulty pixels or window emissivity has been attempted, so absolute and inter-image temperature differences may be in error by several degrees.

Much of this analysis assumes that the emissivity of snow is close to 1 and is relatively invariant across the area of interest irrespective of incidence angle. For fine- and medium-grained snow, field measurements indicate that this is not an unreasonable assumption (Hori and others, 2006). However, the variation of night time temperature for the slope surface characteristic over non-crevassed regions indicates this assumption is not wholly true. In the 03:00 example image (Fig. 2), there are cooler areas beyond the crevasse field that appear to be related to the surface slope. This relationship is highlighted in the night section of the slope-temperature plot of Fig. 8b. The slopes which had a high incidence angle with respect to the camera view returned colder night time temperatures. It seems the incidence angle and hence the emissivity affected the thermal camera temperatures overnight, but not

https://doi.org/10.1017/jog.2025.7 Published online by Cambridge University Press

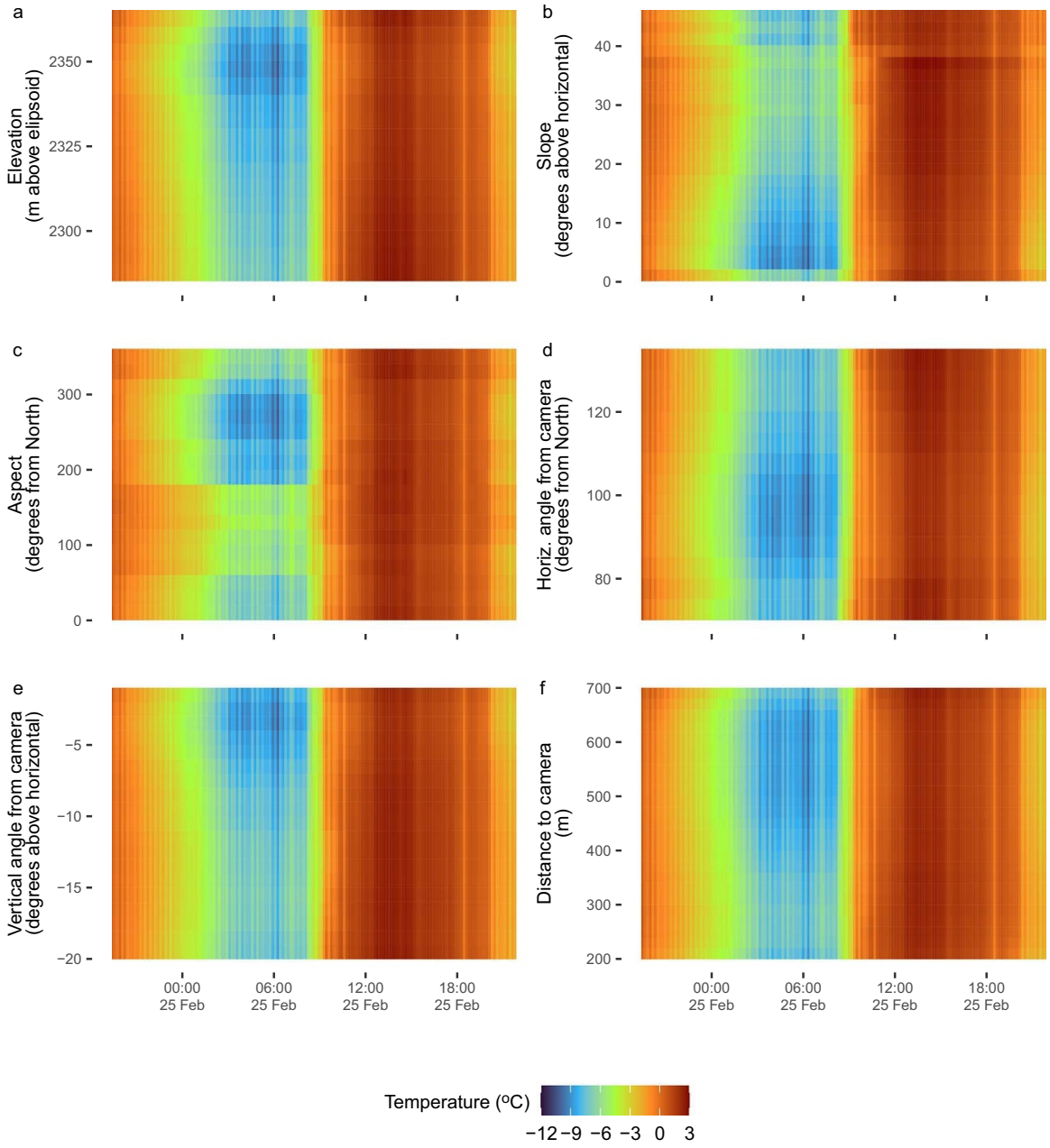


Figure 8. Variation of surface temperature over time for non-crevassed areas within the area of interest for different surface characteristics: (a) elevation, (b) slope, (c) aspect, (d) horizontal angle from camera, (e) vertical angle from camera and (f) distance to camera.

during the day. During a clear night, the previous day's melting surface freezes, creating a sun crust. The emissivity of a sun crust surface is slightly lower than snow but also has a greater variation with incidence angle. Hori and others (2006) measured an emissivity drop of 0.03 for the sun crust when the incidence angle changed from 60 to 75°. For outgoing longwave radiation of 300 W m^{-2}, this emissivity variation would be observed by the infrared camera as a temperature change of 2°C. This variation in emissivity with respect to the viewing angle provides an explanation for the apparent cooler night time temperatures associated with the low slopes. This means that in those low slope areas, distant from the camera, the thermal imagery temperatures will be an underestimate of the true surface temperature.

The other surface characteristic with obvious night time temperature variation was aspect, as shown in Fig. 8c. Aspects between 90 and 180° show as being warmer. Most of the areas of interest had an aspect between 200 and 275° (Fig. 7c). The only areas with aspects less than 180° are around crevasse edges. This indicates the low aspect angles are another proxy for crevasse proximity, which explains their night time relative warmth. This aspect-to-crevasse (and hence aspect-to-temperature) relationship is only relevant to this particular study site, where the non-crevassed areas happen to be associated with a small range of aspects.

The observed dust on the glacier surface caused no robust change in surface temperature compared to no dust surfaces (Fig. 4c). This is despite the impact dust would have on albedo and

https://doi.org/10.1017/jog.2025.7 Published online by Cambridge University Press

emissivity (e.g. Oerlemans and others, 2009; Di Mauro and others, 2015). During the day, temperatures were capped at 0°C from melting, so even if the dust-induced albedo change was increasing energy receipt, it was not reflected in an increased temperature. During the night, any emissivity effects of the dust were not able to be distinguished beyond the intra-image temperature uncertainty of the thermal images. A 09:00 spike in dust/no dust temperature difference indicated a dust effect, but a comparison of a variety of surface sample temperatures returned amplified differences (both positive and negative) around 09:00 irrespective of the dust cover. These 09:00 differences were interpreted as artefacts of slight timing variations in the rapidly warming measurements, not as a robust indication of a dust effect.

Different surface types can also affect the thermal temperature. Rinker (1975) showed that compacted snow could present a warm signal, which they attributed to improved heat conduction from the sub-surface snow. The thermally imaged crevasse walls were generally compacted snow, firn or ice and so would generally have higher conductance than the non-crevassed glacier surfaces that were covered in snow from the previous winter. This would suggest that the crevasse wall temperatures were affected more by the general glacier-ice temperature than the non-crevassed glacier surfaces were. For the temperate Tasman Glacier, the main body of the glacier is assumed to be at 0°C . Overnight, any heightened conduction with the surrounding ice would reduce the cooling effect from outgoing longwave radiation. Classification of different crevasse wall surfaces was not carried out, so identifying if this effect was measurable from the thermal imagery did not occur. Quantifying the magnitude of different snow and ice conductivity on surface temperatures provides a potential avenue for future research.

Crevasses can accentuate shortwave radiation receipt through repeated reflections (Pfeffer and Bretherton, 1987; Cathles and others, 2011). Detecting this effect with a thermal camera over snow would require the difference in shortwave to result in a difference in surface temperature, a condition not met during melting when surface temperature-to-energy flux relationships breakdown. In addition, any increase in shortwave energy within the crevasse needs to be distinguished from reduced turbulent energy fluxes resulting from the wind sheltering within the crevasses. During the daytime, melting was occurring, limiting the surface temperature variance, highlighted by the consistent temperature across the area of interest, largely irrespective of surface characteristic, dust cover or crevassing. This daytime melt sets a maximum possible surface temperature and prevents the infrared camera from clearly observing the impact of shortwave radiation receipt variation across the area of interest. In Fig. 4b, the difference series has a positive spike at 09:00, indicating the non-crevassed sample location was warming ahead of the crevasse sample location, which might be interpreted as the impact of different shortwave receipts. As described earlier with respect to the dust/no dust temperature samples, comparisons of multiple nearby sample points returned varying 09:00 spikes, irrespective of crevasse classification. As a result, the 09:00 effects have been interpreted as an artefact of comparing time series during rapid temperature changes, effectively amplifying any small differences in temperature or timing which cannot be equivocally attributed to shortwave variations. Repeating the experiment in early winter, when temperatures are colder, the melt is not occurring, but crevasses are still open, which might help to improve observations of the solar effect.

The more notable effect observed from the thermal images was the reduced overnight cooling around the crevassed areas. At night, the energy balance is greatly simplified by the lack of shortwave radiation. At these times, loss of heat due to longwave emission can dominate the energy balance of the snow surface (Garvelmann and others, 2014). Within crevasses, this longwave radiation is not emitted away from the glacier but is received by opposing crevasse walls. This receipt of longwave energy offsets the loss, thereby keeping the temperature of the crevasse walls higher compared to the sky-exposed glacier surfaces. This is most noticeable on clear-sky nights as incoming longwave energy from the air is reduced by about 30 % compared to overcast conditions (Plüss and Ohmura, 1997). The crevasses reduced longwave emission away from the glacier surface seems likely to be the primary effect that is causing their relative warmth or, at least, reduced cooling. Measurement of longwave radiation fluxes adjacent to crevasse walls would enable the hypothesis to be tested and the magnitude of the effect to be quantified. Similarly, a full simulation of the energy exchanges associated with the crevasses would clarify the primary processes and their relative magnitudes (e.g. Plüss and Ohmura, 1997).

Purdie and others (2022) described wind transporting air overlying the glacier surface into crevasses. These pulses of warm surface air were found to increase crevasse air temperatures by up to 2 degrees and helped maintain positive temperatures at depth through the night (Purdie and others, 2022, Fig. 10b, p. 419). This overnight trapped warm air provides an additional source of energy for sensible heat transfer into the crevasse walls.

Increased meltwater within a crevasse during the day from either crevasse wall melting or percolation from adjacent snow surfaces can also affect surface temperatures. Flowing meltwater may be considered an energy flux, moving energy from snow melt areas (Hock, 2005). Meltwater is also an energy sink which can cause a break in energy-temperature relationships, most commonly during its generation at 0°C but also by delaying the drop in temperature as energy is used in the latent heat of freezing. On horizontal surfaces meltwater tends to percolate into the snow away from the surface. For near-vertical walls within the crevasse, meltwater tends to flow down, staying on the wall surface. Water-dripping sound recordings were obtained from within one of the crevasses for an entire night in the summer of 2021. This indicates that there is not always sufficient energy being lost overnight from the crevasse walls to freeze all the meltwater. Whether the water was from the crevasse walls melting or had percolated from elsewhere was not determined but would make an interesting study. As well as being a conduit for meltwater, crevasses increased shortwave radiation receipt compared to non-crevassed surfaces would further increase the potential for meltwater, accentuating its effect in delaying cooling overnight. Increased liquid water drainage in a Greenland crevasse, as evidenced by a general coating of drip ice observed on the crevasse walls, was used as part of the explanation for why ice layers in the firn thinned as they approached the crevasse (Meier and others, 1957). If night time water freezing within crevasses was a dominant effect on elevated crevasse wall temperatures, then observed night wall temperatures would hold steady as surface water froze before cooling. For the example in Fig. 4b, there is no obvious delay in the onset of cooling overnight for either of the sample sites. This indicates meltwater freezing is unlikely to be a dominant effect on crevasse wall temperatures but does not disprove that it is occurring.

While the plan view of a crevasse may be small, its actual wall surface area is many times larger (e.g. a 6 m deep crevasse, 2 m wide has 6 times more wall area than the area of its opening). If the reduction in overnight energy loss within a crevasse is 1/6th of sky-exposed surfaces then the difference is offset by the increased surface area. For this to be true, the crevasse wall temperature

https://doi.org/10.1017/jog.2025.7 Published online by Cambridge University Press

would have to have only dropped by 1°C overnight rather than the 4°C observed. This indicates that, despite the crevasse walls being warmer, the impact of their high surface area is to have a net reduction in energy for the glacier and that ignoring crevasses will underestimate the overall outgoing longwave energy.

In terms of practicality of the experimental setup, the use of a ground-based thermal infrared camera in a relatively remote location is not without its challenges. The equipment itself was only really suitable for relatively short manual transport and fine-weather installation. For the New Zealand alpine climate of regular high winds and precipitation, a longer-term thermal camera installation overlooking a glacier would be a logistical and engineering challenge. The attributes and limitations of an Optris thermal camera system for this kind of application are well described in Arioli and others (2024). For crevasses in particular, the camera resolution (2 m) at the outer edge of the area of interest was larger than the width of many crevasses, particularly as they were being viewed at an oblique angle. This limitation, together with the impact of shallow camera view angles on emissivity and the shadowing of crevasses walls, suggests that measurement setups will be best where images are taken with steep view angles to the crevasses of interest.

6. Conclusion

The thermal infrared images collected over 26 hours highlight the impact crevasses have on the surface temperature fields on an alpine glacier. Compared to non-crevassed glacier surfaces, crevasse walls cooled at a slower rate overnight becoming relatively warmer. This temperature difference disappeared during the day as all surface types began melting. The effect of the crevasses on temperature was greater than what could be attributed to slope effects. While we conclude that the overnight temperature differential is primarily associated with the reabsorption of emitted longwave radiation by opposing crevasse walls, other energy sources may also play a role, as indicated by observations of meltwater movement within crevasses, previous observations of warm air entrapment by crevasses, and differences in thermal conductivity of crevasse walls compared to non-crevassed surfaces. For simple mass balance models that ignore crevasses, the default assumption is that net crevasse energy exchange equals the energy exchange for a sky-exposed surface equal in area to the crevasse opening. Shortwave energy modelling indicates that ignoring crevasses leads to an underestimation of daytime energy receipt. Our observations indicate that ignoring crevasses will also lead to a bias in night time energy receipt from longwave radiation. The bias likely leads to overestimation of energy receipt, as despite crevasses appearing warmer, their greater surface area compensates for the reduced outward energy flux.

The results presented here are a snapshot in time, which showcase important processes relevant to all alpine glaciers, where air temperature over the glacier surface can at times be positive. The magnitude of the impact of crevasses on a glacier's energy balance will be related to the number of exposed crevasses, which can vary considerably from glacier to glacier and season to season. Further surface temperature observations of crevasse fields from a range of glaciers during different seasons and weather conditions will help determine the relative importance of different energy fluxes in crevassed terrain. These will enable resolving or parameterising crevasse effects within glacier mass balance assessments, thereby raising confidence and lowering uncertainty in glacier melt models and climate change projections.

Acknowledgements. This research is supported by the Marsden Fund Council from Government funding, managed by Royal Society Te Apārangi, grant number MFP-UOC1804; the Ministry of Business, Innovation and Employment (MBIE), New Zealand, grant number ANTA1801, and by the Royal Society of New Zealand grant number RDF-UOC1701. We also acknowledge the support of the Department of Conservation for permitting research within Aoraki Mt Cook National Park (research permit 98093-GEO). Transport to and from the field site was enabled by Heliworks. Field safety was provided by Jane Morris IFMGA. Justin Harrison provided technical support for equipment. We acknowledge the two anonymous reviewers for their helpful and well-considered suggestions to improve the manuscript.

References

Apogee (2020) *Owner's Manual Net Radiometer Model SN-500-SS*. Technical Report. Logan, UT: Apogee Instruments.

Arioli S and 6 others (2024) Time series of alpine snow surface radiative-temperature maps from high-precision thermal-infrared imaging. *Earth System Science Data* **16**, 3913–3934. doi: 10.5194/essd-16-3913-2024

Arnold NS Rees WG, Hodson AJ and Kohler J (2006) Topographic controls on the surface energy balance of a high Arctic valley glacier. *Journal of Geophysical Research: Earth Surface* **111**, 1–15. doi: 10.1029/2005JF000426

Aubry-Wake C and 7 others (2015) Measuring glacier surface temperatures with ground-based thermal infrared imaging. *Geophysical Research Letters* **42**, 8489–8497. doi: 10.1002/2015GL065321

Beyer RA, Alexandrov O and McMichael S (2018) The Ames stereo pipeline: NASA's open source software for deriving and processing terrain data. *Earth and Space Science* **5**, 537–548. doi: 10.1029/2018EA000409

Bhardwaj A, Sam L, Singh S and Kumar R (2016) Automated detection and temporal monitoring of crevasses using remote sensing and their implications for glacier dynamics. *Annals of Glaciology* **57**(71), 81–91. doi: 10.3189/2016AoG71A496

Bilish SP, McGowan HA and Callow JN (2018) Energy balance and snowmelt drivers of a marginal subalpine snowpack. *Hydrological Processes* **32**, 3837–3851. doi: 10.1002/hyp.13293

Bowen M and Vincent RF (2021) An assessment of the spatial extent of polar dust using satellite thermal data. *Scientific Reports* **11**, 901. doi: 10.1038/s41598-020-79825-7

Cathles LM, Abbot DS, Bassis JN and MacAyeal DR (2011) Modeling surface-roughness/solar-ablation feedback: application to small-scale surface channels and crevasses of the Greenland ice sheet. *Annals of Glaciology* **52**(59), 99–108. doi: 10.3189/172756411799096268

Chinn TJ (2001) Distribution of the glacial water resources of New Zealand. *Journal of Hydrology (NZ)* **40**, 139–187.

Christen A, Meier F and Scherer D (2012) High-frequency fluctuations of surface temperatures in an urban environment. *Theoretical and Applied Climatology* **108**, 301–324. doi: 10.1007/s00704-011-0521-x

Colgan W and 6 others (2016) Glacier crevasses: observations, models, and mass balance implications. *Reviews of Geophysics* **54**, 119–161. doi: 10.1002/2015RG000504

Cook JC (1956) Some observations in a northwest Greenland crevasse. *Eos, Transactions American Geophysical Union* **37**, 715–718. doi: 10.1029/TR037i006p00715

Cotton C (1941) Moraines and outwash of the Tasman Glacier. *Transactions of the Royal Society of New Zealand* **71**, 204–207.

Di Mauro B and 6 others (2015) Mineral dust impact on snow radiative properties in the European Alps combining ground, UAV, and satellite observations. *Journal of Geophysical Research: Atmospheres* **120**, 6080–6097. doi: 10.1002/2015JD023287

Dozier J and Warren SG (1982) Effect of viewing angle on the infrared brightness temperature of snow. *Water Resources Research* **18**, 1424–1434. doi: 10.1029/WR018i005p01424

Garvelmann J, Pohl S and Weiler M (2014) Variability of observed energy fluxes during rain-on-snow and clear sky snowmelt in a midlatitude mountain environment. *Journal of Hydrometeorology* **15**, 1220–1237. doi: 10.1175/JHM-D-13-0187.1

Harrison WD, Echelmeyer KA and Larsen CF (1998) Measurement of temperature in a margin of Ice Stream B, Antarctica: implications for margin migration and lateral drag. *Journal of Glaciology* **44**(148), 615–624. doi: 10.3189/S0022143000002112

Hijmans RJ (2024) Terra: Spatial Data Analysis. R package version 1.7-78. Available at https://CRAN.R-project.org/package=terra (accessed 11 January 2024).

Hock R (2005) Glacier melt: a review of processes and their modelling. *Progress in Physical Geography: Earth and Environment* **29**, 362–391. doi: 10.1191/0309133305pp453ra

Hock R and 7 others (2019) GlacierMIP – a model intercomparison of global-scale glacier mass-balance models and projections. *Journal of Glaciology* **65**(251), 453–467. doi: 10.1017/jog.2019.22

Hori M and 10 others (2006) In-situ measured spectral directional emissivity of snow and ice in the 8–14 μm atmospheric window. *Remote Sensing of Environment* **100**, 486–502. doi: 10.1016/j.rse.2005.11.001

Kerr T, Owens I and Henderson R (2011) The precipitation distribution in the Lake Pukaki catchment. *Journal of Hydrology (NZ)* **50**, 361–382

Kinar NJ and Pomeroy JW (2015) Measurement of the physical properties of the snowpack. *Reviews of Geophysics* **53**, 481–544. doi: 10.1002/2015RG000481

Kirkbride M (1995) Ice flow vectors on the debris-mantled Tasman Glacier, 1957–1986. *Geografiska Annaler* **77**, 147–157. doi: 10.1080/04353676.1995.11880435

Kraaijenbrink PDA and 6 others (2018) Mapping surface temperatures on a debris-covered glacier with an unmanned aerial vehicle. *Frontiers in Earth Science* **6**, 1–19, doi: 10.3389/feart.2018.00064

Lendenfeld R (1884) *Der Tasman-Gletscher und seine Umrandung 75*, Gotha, Germany: Julius Perthes, vol. 16, p. 80.

Litwa M (2010) Influence of angle of view on temperature measurements using thermovision camera. *IEEE Sensors Journal* **10**, 1552–1554. doi: 10.1109/JSEN.2010.2045651

Lorrey AM and 9 others (2022) Southern Alps equilibrium line altitudes: four decades of observations show coherent glacier-climate responses and a rising snowline trend. *Journal of Glaciology* **68**(272), 1127–1140. doi: 10.1017/jog.2022.27

Meier F, Scherer D, Richters J and Christen A (2011) Atmospheric correction of thermal-infrared imagery of the 3-D urban environment acquired in oblique viewing geometry. *Atmospheric Measurement Techniques* **4**, 909–922. doi: 10.5194/amt-4-909-2011

Meier MF, Conel J, Hoerni J, Melbourne W, Pings Jr C Walker P (1957) Preliminary study of crevasse formation: Blue Ice Valley, Greenland, 1955. SIPRE Report 38, Snow Ice and Permafrost Research Establishment. US Army Corps of Engineers

Oerlemans J, Giesen RH and van den Broeke MR (2009) Retreating alpine glaciers: increased melt rates due to accumulation of dust (Vadret da Morteratsch, Switzerland). *Journal of Glaciology* **55**(192), 729–736. doi: 10.3189/002214309789470969

Oke TR (1987) *Boundary Layer Climates*. London: Routledge. ISBN 978-0-415-04319-9.

Olson M, Rupper S and Shean DE (2019) Terrain induced biases in clear-sky shortwave radiation due to digital elevation model resolution for glaciers in complex terrain. *Frontiers in Earth Science* **7**, 1–12, doi: 10.3389/feart.2019.00216

Optris (2020) *Optris PI operator's manual. Data Sheet Optris PI-MA-E2020-08-A*. Berlin: Optris GmbH.

Pestana S and 7 others (2019) Bias correction of airborne thermal infrared observations over forests using melting snow. *Water Resources Research* **55**, 331–343. doi: 10.5194/tc-16-559-2022

Pfeffer WT and Bretherton CS (1987) The effect of crevasses on the solar heating of a glacier surface. In *The Physical Basis of Ice Sheet Modelling, General Assembly of the International Union of Geodesy and Geophysics, Vancouver Symposium,* IAHS, pp. 191–205.

Pings CJ (1961) Temperature distribution near a crevasse. *Journal of Glaciology* **3**(30), 985–996. doi: 10.3189/S0022143000017391

Pings CJ (1963) Heat flux distribution near a crevasse. *Journal of Glaciology* **4**(34), 461–465. doi: 10.3189/S002214300002788X

Plüss C and Ohmura A (1997) Longwave radiation on snow-covered mountainous surfaces. *Journal of Applied Meteorology and Climatology* **36**, 818–824. doi: 10.1175/1520-0450-36.6.818

Purdie H and 6 others (2011) Interannual variability in net accumulation on Tasman Glacier and its relationship with climate. *Global and Planetary Change* **77**, 3–4. doi: 10.1016/j.gloplacha.2011.04.004

Purdie H, Anderson B, Mackintosh A and Lawson W (2018) Revisiting glaciological measurements on Haupapa/Tasman Glacier, New Zealand, in a contemporary context. *Geografiska Annaler: Series A, Physical Geography* **100**, 351–369. doi: 10.1080/04353676.2018.1522958

Purdie H and Kerr T (2018) Aoraki Mount Cook: environmental change on an iconic mountaineering route. *Mountain Research and Development* **38**, 364–380. doi: 10.1659/MRD-JOURNAL-D-18-00042.1

Purdie H, Zawar-Reza P, Katurji M, Schumacher B, Kerr T and Bealing P (2022) Variability in the vertical temperature profile within crevasses at an alpine glacier. *Journal of Glaciology* **69**(274), 410–424. doi: 10.1017/jog.2022.73

Purdie J and Fitzharris B (1999) Processes and rates of ice loss at the terminus of Tasman Glacier, New Zealand. *Global and Planetary Change* **22**, 79–91. doi: 10.1016/S0921-8181(99)00027-2

R Core Team (2021) *R: A Language and Environment for Statistical Computing*. Vienna: R Foundation for Statistical Computing.

Rinker JN (1975) Airborne infrared thermal detection of caves and crevasses. *Photrgrammetric Engineering and Remote Sensing* **41**, 1391–1400

Robledano A, Picard G, Arnaud L, Larue F and Ollivier I (2022) Modelling surface temperature and radiation budget of snow-covered complex terrain. *The Cryosphere* **16**, 559–579. doi: 10.5194/tc-16-559-2022

Röhl K (2008) Characteristics and evolution of supraglacial ponds on debris-covered Tasman Glacier, New Zealand. *Journal of Glaciology* **54**(188), 867–880. doi: 10.3189/002214308787779861

Rossini M and 8 others (2023) Mapping surface features of an alpine glacier through multispectral and thermal drone surveys. *Remote Sensing* **15**, 3429 10.3390/rs15133429

Skinner B (1964) Measurement of twentieth century ice loss on the Tasman Glacier, New Zealand. *New Zealand Journal of Geology and Geophysics* **7**, 796–803. doi: 10.1080/00288306.1964.10428130

Winton VHL and 9 others (2024) New Zealand Southern Alps blanketed by red Australian dust during 2019/2020 severe bushfire and dust event. *Geophysical Research Letters* **51**, 1–13. doi: 10.1029/2024GL112782